Operando Evidence for a Universal Oxygen Evolution Mechanism on Thermal and Electrochemical Iridium Oxides

Viktoriia A. Saveleva[a*], *Li Wang*[b], *Detre Teschner*[c,d], *Travis Jones*[c], *Aldo S. Gago*[b], *K. Andreas Friedrich*[b,e], *Spyridon Zafeiratos*[a], *Robert Schlögl*[c,d], *Elena R. Savinova*[a,†]

[a]Institut de Chimie et Procédés pour l'Energie, l'Environnement et la Santé, UMR 7515 du CNRS-UdS 25 Rue Becquerel, 67087 Strasbourg, France

[b]Institute of Engineering Thermodynamics, German Aerospace Center (DLR), Pfaffenwaldring 38-40, 70569 Stuttgart, Germany

[c]Departement of Inorganic Chemistry, Fritz-Haber-Institut der Max-Planck-Gesellschaft Faradayweg 4–6, 14195 Berlin, Germany

[d]Department of Heterogeneous Reactions, Max-Planck-Institut für Chemische Energiekonversion, Stiftstr. 34-36, 45470, Mülheim a. d. Ruhr, Germany

[*]Current address: Electrochemistry Laboratory, Paul Scherrer Institut, 5232 Villigen, Switzerland

[†]Corresponding author. Phone: ++33(0)3 68 85 27 39. Fax: ++33(0)3 68 85 27 61

E-mail: elena.savinova@unistra.fr

[e]Institute of Energy Storage, University of Stuttgart, Pfaffenwaldring 31, 70569 Stuttgart, Germany

Progress in the development of the proton exchange membrane (PEM) water electrolysis technology requires decreasing the anode overpotential, where the sluggish multistep oxygen evolution reaction (OER) occurs. This calls for the understanding of the nature of the active OER sites and reaction intermediates, which are still being debated. In this work, we apply synchrotron radiation – based near ambient pressure X-ray photoelectron and absorption spectroscopies under *operando* conditions in order to unveil the nature of the reaction intermediates and shed light on the OER mechanism on electrocatalysts most widely used in PEM electrolyzers - electrochemical and thermal iridium oxides. The analysis of the O K-edge and Ir4f spectra backed by density functional calculations reveals a universal oxygen anion red-ox mechanism regardless of the nature (electrochemical or thermal) of the iridium oxide. The formation of molecular oxygen is considered to occur through a chemical step from the electrophilic O^{I-} species, which itself is formed in an electrochemical step.

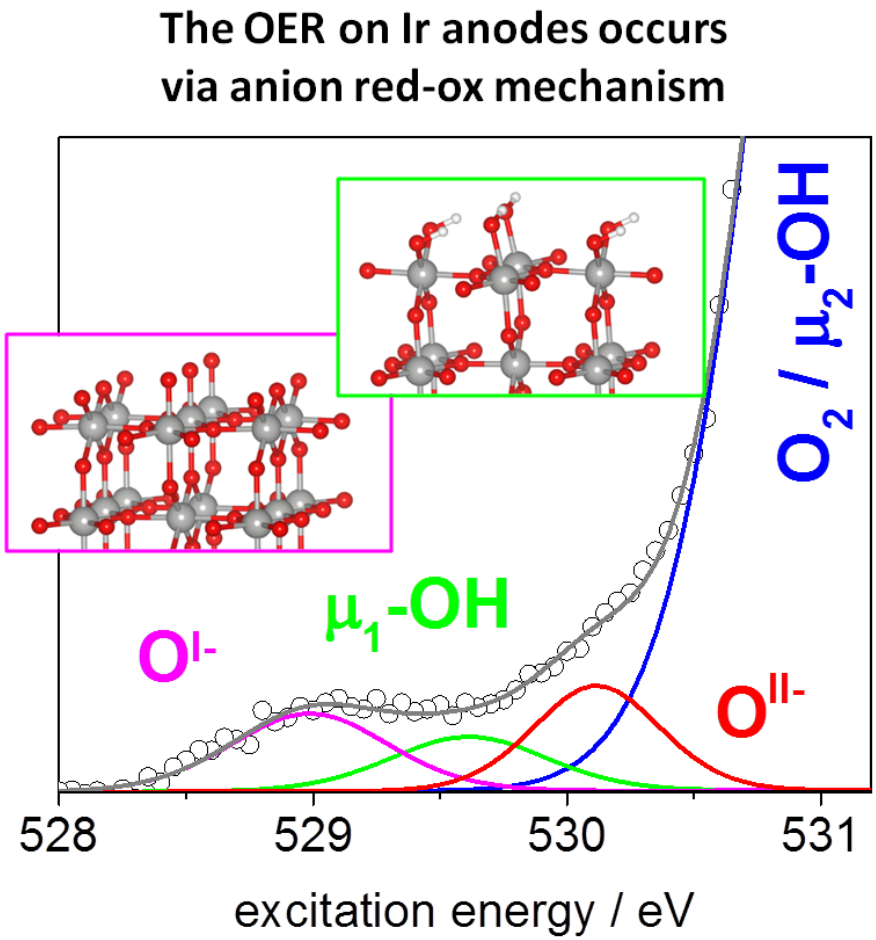

Table of contents graphic

KEYWORDS: Oxygen evolution reaction (OER), Proton Exchange Membrane (PEM) water electrolysis, Near-Ambient Pressure XPS (NAP-XPS), soft X-ray absorption spectroscopy, O K-edge, active sites

Water splitting via proton exchange membrane (PEM) electrolysis is currently considered the most viable option for the conversion and storage of surplus electricity from renewable sources (photovoltaic panels or wind mills) due to its high efficiency, high operating current density, compactness, operational safety and its capacity to adapt to variations in electricity input. State-of-the-art anodes for PEM electrolyzers are based on iridium (thermally or electrochemically oxidized)[1], thus wide dissemination of the PEM technology will raise the issue of its high cost and limited resources. Significant effort has recently been focused on the development of oxygen evolution reaction (OER) catalysts with low Ir loading and high mass-weighted catalytic activity [2–4]. Further prospects in the catalyst development depend on progress in the understanding of the mechanism of the OER, uncovering the nature of the active sites, and detecting key reactive intermediates of this complex electrocatalytic process. Despite several decades of intensive research and significant progress, the mechanism of heterogeneous electrocatalytic OER is still insufficiently understood largely due to the difficulties in unveiling the nature of the active sites *under the reaction conditions* and detecting reaction intermediates. Kötz et al.[5] studied the OER on electrochemically oxidized Ir metal anodes using *ex situ* photoelectron spectroscopy at electrodes withdrawn from the electrolyte and came up with a catalytic cycle comprising Ir (IV) – Ir (V) – Ir (VI) red-ox transitions. Similar catalytic cycle was discussed in a recent work of Kasian et al.[6] on the grounds of a gaseous Ir corrosion product detected at high potentials. Formation of a high valence Ir (V) intermediate was also proposed in the recent *in situ* study of Casalongue et al.[7] based on a near-ambient pressure X-ray photoelectron spectroscopy (NAP-XPS) study of a membrane electrode assembly (MEA) comprising IrO_2 particles. Minguzzi et al.[8] applied *in situ* X-ray absorption spectroscopy to study electrochemically grown oxide films on Ir and concluded that during the OER Ir is present in both the Ir (III) and Ir (V) oxidation

states. However, Pfeifer et al.[9] challenged this conclusion suggesting that the OER on Ir occurs via the oxygen anion rather than metal cation red-ox cycle whereby electron-deficient electrophilic oxygen (denoted as an O^{I-} species) is formed as a reactive intermediate. The latter was detected *in situ* using X-ray absorption near edge structure (XANES) spectroscopy. Participation of lattice oxygen in the OER and formation of O^{I-} intermediates were also suggested on perovskite oxides under high temperature operation by Mueller et al.[10]

The controversies in the understanding of the nature of active sites and intermediates impact the current catalyst development. They could originate from the different types of catalytically active phase (electrochemically grown Ir oxide films or IrO_2 with a rutile structure obtained by high temperature oxidation of Ir), various electrode structures (polycrystalline electrodes, sputtered films, nanoparticles), reactive environments (solid electrodes in contact with aqueous acid solutions or MEAs comprised of catalytic particles deposited on PEMs), applied potential intervals and characteristic measurement times. It is well accepted that electrochemical Ir and Ru oxides outperform the corresponding crystalline rutile-type oxides[11–15], which is likely to be related to the differences in their composition (hydrous oxide *vs*. oxide) and structure (amorphous *vs*. crystalline). While the relationship between the electrocatalytic activity and the presence of Ir hydroxo-species on the surface has been established,[4] it is still unclear whether the OER on thermal and electrochemical oxides follows the same mechanism.

Here we present a comparative *operando* photoemission study of two types of Ir anode electrocatalysts: (i) Ir metal nanoparticles covered by an electrochemically grown thin oxide layer (in what follows labeled as $Ir@IrO_x$) and (ii) IrO_2 synthesized by thermal oxidation of metal nanoparticles. In order to reproduce, as close as possible, the environment experienced by the catalysts in a commercial PEM electrolyzer, both catalysts were sprayed on PEMs to produce

MEAs. These were subsequently studied using soft X-ray absorption spectroscopy at the O K-edge and by NAP-XPS at the Ir4f and O1s core levels, under the same operating conditions, to detect possible red-ox transitions of O anions and/or Ir cations during the OER. The purpose of this work is to clarify whether the OER occurs on the same active sites via the same reactive intermediates on the "electrochemical" and on the "thermal" oxide and thus reconcile some of the literature controversies.

The catalyst samples were prepared by direct reduction of an anhydrous Ir salt in water-free conditions resulting in metallic Ir particles of ca. 2 nm diameter as described in Ref. [2] (see Scanning Transmission Electron Microscopy (STEM) images in Figure S1). IrO_2 nanoparticles were obtained by thermal treatment of these Ir particles under air at 490 °C ("thermal" oxide), whereby the formation of a stable rutile-type oxide was confirmed by X-ray diffraction analysis (Figure S2). STEM images of thermally obtained rutile-type IrO_2 showed rod-shape particles with a mean width of ca. 5.5 nm and a length of ca. 15.0 nm. Cyclic voltammograms (CV), acquired with a three-electrode electrochemical cell in the presence of 0.05 M H_2SO_4, are shown in Figure 1A and Figure S3. The results show anodic and cathodic peaks in the potential interval from 0.2 to 1.3 V *vs.* reversible hydrogen electrode (RHE) with much higher currents for Ir@IrO_x with respect to the IrO_2 sample, which cannot be correlated to their differences in particle size or estimated surface area (Supporting Information). Such increase in the current densities is also observed in the CVs measured in the NAP-XPS chamber but is less notorious (Figure S4). In agreement with the literature data[16,17] higher pseudocapacitance of the amorphous electrochemical oxide may be attributed to red-ox transitions coupled with proton intercalation/deintercalation in sub-surface (bulk), while for crystalline IrO_2 it only occurs on the surface, probably at specific surface sites. This observation will be further corroborated

considering Ir4f XP data. The OER activities of Ir@IrO_x and IrO_2 powders tested in a three-electrode electrochemical cell in the presence of 0.05 M H_2SO_4 confirm the higher mass activity of Ir@IrO_x vs. IrO_2 nanoparticles (Figure 1B).

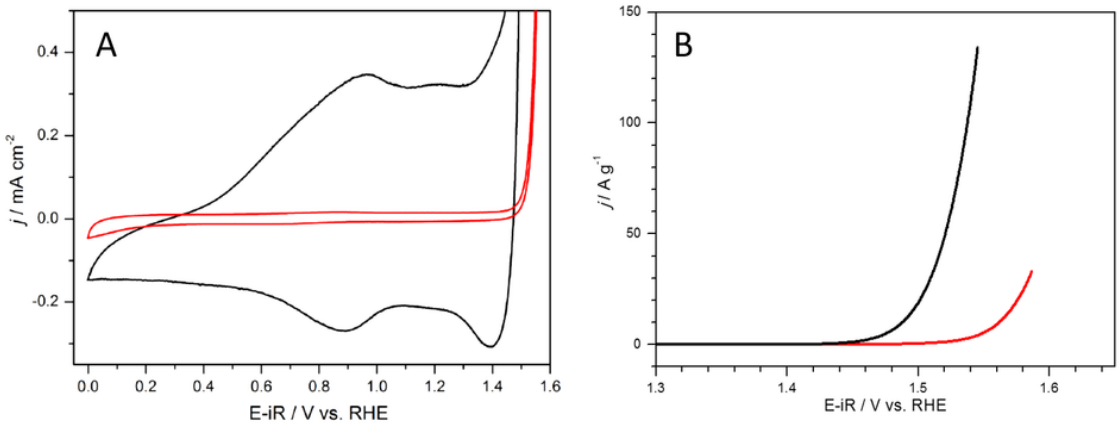

Figure 1. Ohmic drop corrected CVs (the 10th cycles are shown) at 20 mV s^{-1} (Panel A) and mass-weighted OER currents acquired at 5 mV s^{-1} (Panel B) for Ir@IrO_x (black) and IrO_2 (red) anodes recorded in N_2-saturated 0.05 M H_2SO_4 at 25 °C and 1600 rpm rotation speed. Catalyst loading was 60 µg cm^{-2}.

The *operando* photoemission studies were performed in a two-electrode configuration under 3 mbar H_2O pressure[18] using MEAs with either IrO_2 or metallic Ir as the working electrode and commercial Pt/C as the counter electrode. Under the OER conditions the latter serves as a dynamic hydrogen electrode (DHE) thus allowing us to define the electrode potential scale[18]. The MEAs were prepared by wet spraying method using Aquivion membranes and ionomers in order to alleviate the effect of the relative humidity on the OER currents[18]. These MEAs were integrated in the electrochemical cell, which was introduced in the spectrometer chamber as described in Refs. [18,19] Electrochemical impedance spectroscopy (EIS) was applied before and after spectroscopic measurements in order to determine the high frequency resistance, which was then used for the Ohmic drop (iR) correction of the electrode potentials. Supplementary

electrochemical measurements performed at different H_2O pressures confirmed little influence of the H_2O pressure on the OER current against the E-iR scale (Figure S5). Before performing spectroelectrochemical measurements, all MEAs were pretreated by cycling in the potential interval from 0 V to 1 V vs. DHE directly in the XPS chamber under 3 mbar water vapor in order to obtain a stable and reproducible surface state. Note that under such a potential cycling a layer of non-stoichiometric oxide is formed on the surface of metallic Ir [5,20,21] which in what follows will be confirmed by the analysis of the Ir4f and O1s XP spectra. For the IrO_2 sample, the potential cycling under 3 mbar water vapor results in a small increase of the contribution of adsorbed OH species in the O1s XP spectra compared to vacuum leaving the Ir4f spectra unchanged (not shown). XANES measurements at the O K-edge and NAP-XPS measurements were realized sequentially without removing the samples from the H_2O vapor ambient by increasing the electrode potential in regular increments (their size depending on the potential interval). For more details, the reader is referred to the Supporting Information.

Density functional theory (DFT) calculations were performed using the Quantum ESPRESSO package version 6.1[22] with the Perdew, Burke, and Ernzerhof exchange and correlation potential. Oxygen K-edge spectra were computed using a one-electron Fermi's golden rule expression.[23,24] Full details are available in Supporting Information.

Figure 2 shows the low excitation energy (pre-edge) region of O K-edge spectra measured in the total electron yield (TEY) mode (panels A,B) for Ir@IrO_x and IrO_2 anodes during oxygen evolution at ~1.5 V (for other potentials the reader is referred to Figures S7, S8), whereas Figure 3 (B) shows O K-edge spectra for various configurations of O and OH species on the (110) surface (Figure 3 A, C) computed using DFT. For the IrO_2 anode the experimental spectra clearly show a *ca*. 530 eV peak and a smaller feature at *ca*. 528.8 eV, which based on the DFT

calculations (Figure 3), and in agreement with Pfeifer et al.[9], can be attributed to bulk lattice oxygen (labeled as O^{II-}) and to electron-deficient electrophilic oxygen species (labeled as O^{I-}), respectively. Our experiments show that the intensity of the O^{I-} species increases with the applied potential once it reaches 1.3 V (Inset of Figure 2 Panel F).

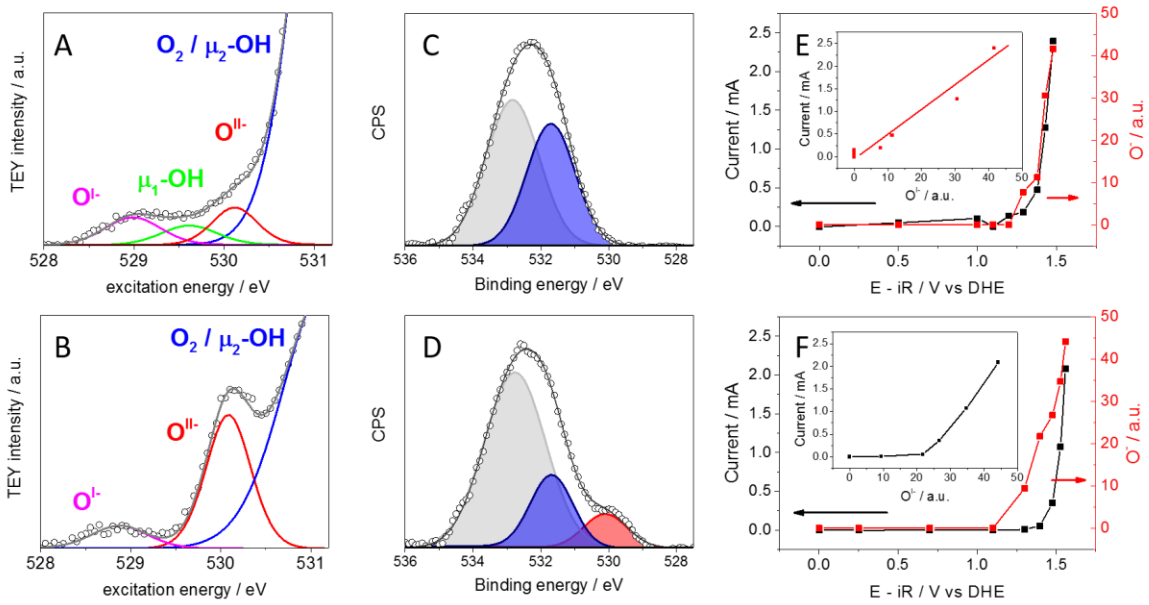

Figure 2. (A, B) Low excitation energy region of the O K-edge spectra recorded under the OER conditions for $Ir@IrO_x$ at E-iR=1.48 V and IrO_2 at E-iR=1.53 V (B). Color codes: O^{I-} (magenta), O^{II-} (red), gas-phase O_2 / μ_2-OH groups (blue), μ_1-OH groups at 529.4 eV (green), experimental points (open circles), fitted curve (gray line). (C,D) O1s XP spectra of $Ir@IrO_x$ (C) and IrO_2 (D) anodes at 0 V, after potential cycling in the interval from 0 to 1.0 V, acquired using photoelectrons with 530 eV kinetic energy. Color codes: lattice oxygen (red), OH and C=O species (blue), water and C-O species (gray), experimental points (open circles), fitted curve (gray line). (E,F) Currents (black) measured 120 s after the application of corresponding potentials and O^{I-} integrated peak intensity (red) versus iR-corrected potential for $Ir@IrO_x$ (E) and IrO_2 (F) anodes. Insets in panels E, F show current versus the O^{I-} integrated peak intensity for $Ir@IrO_x$ (red) and IrO_2 (black) anodes. Measurements were performed at RT under 3 mbar water vapor.

DFT calculations indicate that low excitation energy O K-edge peaks (μ_1-O and μ_2-O in Figure 3) can be created by deprotonation of OH groups at both cus (coordinatively unsaturated) and bridge position (Figure 3). Note that the white line intensity of the O K-edge resonance increases

as the edge position decreases. When we assess the net Löwdin charge (integrated number of occupied p electrons) of various oxygen species, we find a rough correlation between the Löwdin charge and the edge position (Figure 3D): the lower the Löwdin charge the lower the edge position. This indicates that the more electrophilic ('hole') character an O species has the lower its edge position. This is the reason why the low excitation energy species is labeled O^{I-}. Note that Figure 3D contains data from many different surface terminations (for details see Supporting Information) and we can see how the species cluster in the diagram. The spread of the Löwdin charge (and the edge position) for a certain species is caused by local effects, like surface termination, H-bonding and neighboring vacancies. Ir vacancies (which could for example be created through Ir dissolution) create O^{I-} or OH species, for the latter, once deprotonated, the Ir defects push hole character onto O, and hence push the white line position down in energy with a concomitant rise in intensity. Similarly, when an O is an H bond acceptor (donor) in H-bonding, the white line position shifts up (down) in energy as a reflection of the hole character. Based on the DFT calculations the O^{I-} species seen experimentally is most likely μ_2-O, because the edge position of μ_1-O is lower. Peaks at 531.0 eV and higher correspond to various OH species (mostly μ_2-OH, see Figure 3A), and the background increase due to water and gas-phase oxygen formed during the OER.

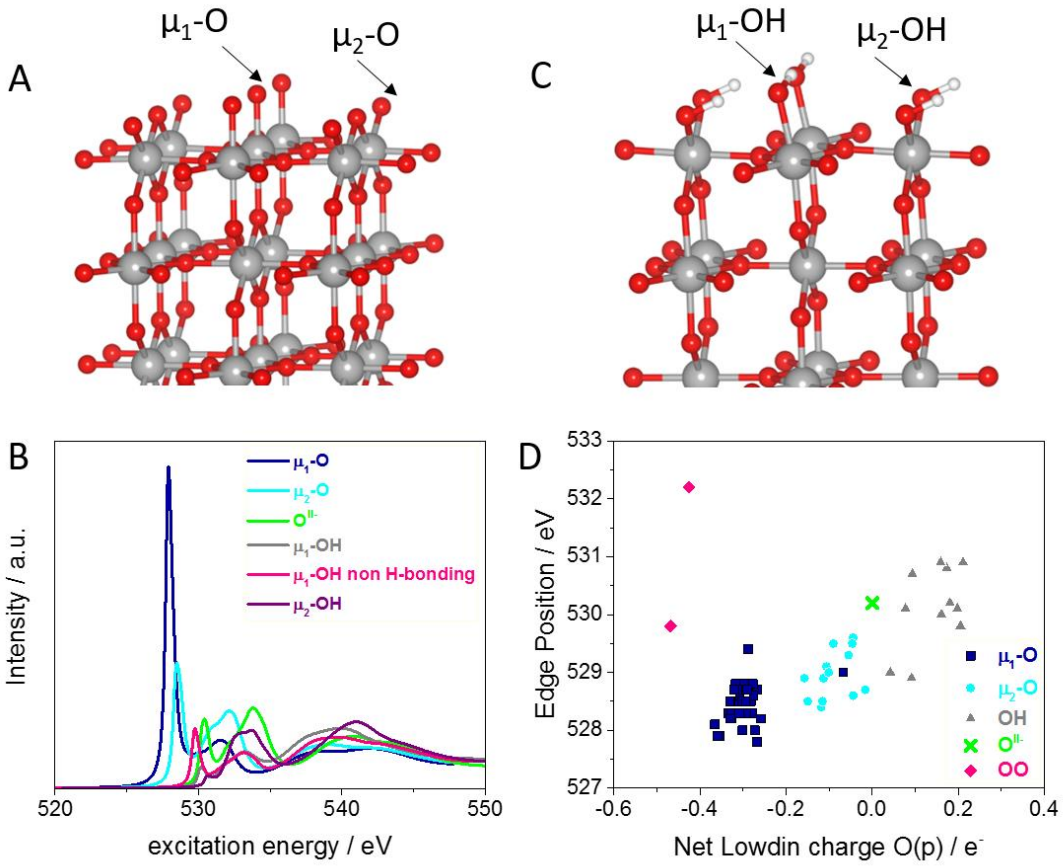

Figure 3: Ball and stick structural model of the (110) IrO_2 surface with O (A) and OH (C) termination. O K-edges (B) computed for μ_1-O and μ_2-O oxygen with O and OH termination as well as for bulk (O^{II-}) anions. Correlation of the O K-edge white line position at various surface terminations as a function of the net Löwdin charge with respect to Löwdin charge of bulk O^{II-} in rutile IrO_2 (D).

It is interesting that the experimental O K-edge spectra observed for Ir@IrO_x are different from those of IrO_2. First, one may notice much lower contribution of the bulk lattice oxygen species in comparison to the IrO_2 anode under the OER conditions (Figure 2A) and even more so before the OER onset where the intensity of the lattice oxygen peak hardly exceeds the noise level (Figure S7). This is explained by different compositions of the electrochemical and the thermal oxide, as confirmed by the analysis of the O1s XP spectra acquired before the measurements of the O K-edge spectra (but after cycling the electrodes in the interval from 0 V to 1 V) and shown in

Figure 2 (C, D), respectively. The fitting of the O1s spectra was done using three components corresponding to bulk lattice oxygen (*ca*. 530.1 eV), OH groups (*ca*. 531.7 eV), which according to the DFT calculations may be attributed to μ_2-OH, and adsorbed water (*ca*. 532.8 eV).[‡] The lattice oxygen component is clearly observed in the O1s spectra of the IrO_2 anode while it is absent for $Ir@IrO_x$, which is in agreement with low intensity of the O^{II-} component in the O K-edge spectra observed below the OER onset and discussed above. One may also notice a higher relative contribution of the μ_2-OH groups in the case of $Ir@IrO_x$, suggesting the formation of a hydrous oxide rather than a rutile-type IrO_2 oxide, but their overlap with oxygen functionalities on carbon (e.g. of the Aquivion membrane) does not allow us to provide a quantitative analysis of the OH/Ir ratio. Second, O K-edge spectra for the $Ir@IrO_x$ anode show an additional peak at 529.6 eV (absent in the IrO_2 O K-edge spectra), which becomes clearly resolvable from the background at E-iR=1.29 V. In order to understand the origin of the 529.6 eV peak, DFT calculations were performed for various surface terminations (OH against O) and considering different types of defects (see Figure 3 and Supporting Information). The feature at 529.6 eV in the O K-edge spectrum is somewhat high for μ_2-O. This low excitation energy resonance also does not appear to be associated with a μ_2-OH, which appears at higher excitation energies. A μ_1-OH species, however, tends to have a white line near 529.6 eV. For instance, a μ_1-OH on the (110) surface appears at 529.7 eV (Figure 3). Such μ_1-OH species are stable at low but are expected to be deprotonated at high potentials. To check this, the O K-edge spectra of the $Ir@IrO_x$ anode were fit with four peaks: at 529.0, 529.6, 530.1 and 531.7 eV, which we attribute to μ_2-O (O^{I-}), μ_1-OH, lattice oxygen O^{II-}, and μ_2-OH respectively (Figure 2 and Figure S7).

[‡] Note that one cannot fully disregard contributions of C=O and C-O species at 531.7 and 532.8 eV to the μ_2-OH and adsorbed water peak respectively.

Plotting the 529.0 eV peak intensity *vs*. the electrode potential shows a remarkable correlation with the OER current growth (see inset in Panel E of Figure 2 where current is plotted against the peak intensity). In the meantime the 529.6 eV peak intensity increases up to ca. 1.38 V, whereby it attains maximum and then decays (Figure S9).

Considering the potential dependence of the peaks and comparing spectroscopic data with the DFT calculations we infer that the 529.6 eV peak corresponds to μ_1-OH, which at potentials above 1.3 V is transformed into the OER intermediate μ_2-O (electrophilic oxygen O^{I-}) with a peak at 529.0 eV. The potential dependence of the O^{I-} peak intensity suggests that deprotonation occurs in an electrochemical step:

$$HO^* \rightarrow O^* + H^+ + e^- \qquad (1),$$

Where O* corresponds to O^{I-} (μ_2-O) species. It should be noted however that the direct product of the deprotonation of μ_1-OH is a μ_1-O. Thus, reaction 1 may not be an elementary step. We see no evidence for the μ_1-O so if it is present it reacts off the surface so quickly that the population is lower than it was as a μ_1-OH. The fact that we did not observe spectroscopic evidence of μ_1-OH on the surface of IrO_2 is in line with the different composition of the thermal *vs*. electrochemical oxide and may suggest a different pathway for the O^{I-} (μ_2-O) formation on the surface of rutile IrO_2 (for example through formation of an Ir vacancy). The linear relationship between the current and the O^{I-} (μ_2-O) peak intensity (see the inset of Panel E in Figure 2) suggests that transformation of μ_2-O into O_2 is independent of the electrode potential and thus occurs in a chemical rather than in an electrochemical step. Following Trasatti[25] this can be tentatively attributed to a recombination step (2) even if other chemical steps (like nucleophilic water attack) cannot be discarded.

$$O^* + O^* \rightarrow O_2 \qquad (2)$$

The observed continuous increase of the O^{I-} intensity in the potential interval from 1.3 up to 1.5 V is not typical for adsorbates located at the surface and suggests that these species may also be formed in the sub-surface region of the catalytic particles in agreement with Pfeifer et al.[26]

We thus propose the electrophilic O^{I-} species to be an intermediate for both the electrochemical and thermal Ir oxide anodes, and that its reactivity depends on the nature of the oxide. While on the electrochemical Ir@IrO_x surface the O^{I-} intermediate undergoes a rapid transformation into oxygen (O_2), on the thermal oxide further steps are slower and may be activated by the electrode potential (note that for the IrO_2 anode the O^{I-} intermediate emerges at potentials below the current rise). These differences are likely to be related to the higher structural flexibility of the amorphous Ir@IrO_x oxide facilitating interaction of species adsorbed at adjacent surface sites (e.g. two O^{I-} intermediates or O^{I-} and adsorbed water molecule), whereby the more "rigid" structure of the thermal oxide does not allow the interaction of adsorbates at adjacent sites. The kind of "induction" period observed in the current *vs*. O^{I-} intensity for IrO_2 may be needed to create enough defects to enable its structural flexibility.

We now turn to the analysis of the Ir4f XP spectra (which were recorded after the series of O K-edge spectra) under various potentials in order to clarify the role of the Ir sites in the OER, and eventually detect red-ox transformations of the surface cations during the OER for the two types of Ir-based anodes. Figures 4A and C represent Ir4f spectra obtained on the Ir@IrO_x anode under two different potentials: 0 and 1.48 V, the latter corresponding to the OER interval (for spectra at other potentials the reader is referred to Figure S11). The fitting was performed using three doublets with $Ir4f_{7/2}$ peak position at 60.85 eV, 62.40 eV and 61.70 eV, which are attributed to Ir (metal), Ir (III) and Ir (IV) components, respectively. Two doublets corresponding to Ir (III) and

Ir (IV) satellites were also employed (for more details the reader is referred to the Supporting Information). The potential-induced evolution of the components is given in Figure 4B. After the initial electrochemical pretreatment the surface of the metallic Ir particles is covered by a Ir (III) / Ir (IV) mixed oxide/hydrous oxide layer in agreement with previous studies on Ir metal electrodes[5]. Increasing the applied potential leads to the diminution of the contribution of the Ir (III) component accompanied by an increase in the Ir (IV) component, in such a way that in the potential interval of the OER the surface is dominated by Ir (IV). Potential reversal back to 0 V results in an increase of the Ir (III) contribution and a decrease of the Ir (IV) component, but does not fully restore the initial spectrum, suggesting an evolution of the composition/structure of the electrochemical oxide during the OER like that reported in previous publications[27]. Decreasing the energy of photoelectrons (and thus increasing the surface-sensitivity similar to what has been done in Ref.[7]) did not reveal any higher oxidation states of Ir on the Ir@IrO_x anodes after their oxidation to Ir (IV) (Figure S12). Decreasing the photon energy resulted in a slight decrease of the metal contribution (from 30 to 17%), confirming formation of the oxide on the surface of the particles, which however was more visible at high potentials. The observed marginal dependence of the component contributions on the photon energy may be attributed to the inhomogeneity of the oxide layer (porous oxide layer) and to the small size of the Ir particles. Based on the intensity ratio of the oxide *vs*. the metal peaks, the effective thickness of the hydrous oxide layer was estimated as ca. 0.5 nm (using SESSA software[28,29]).

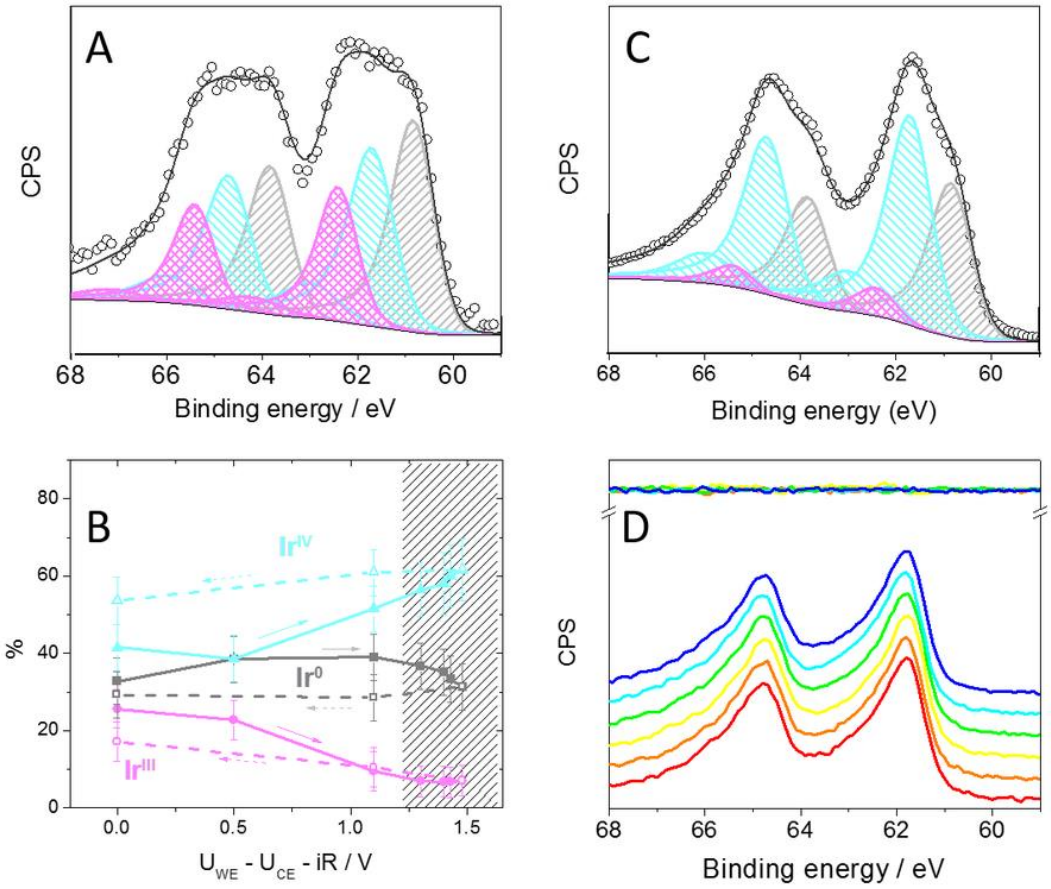

Figure 4.(A,C) Ir4f XP spectra for Ir@IrO_x anode at E-iR=0 V (A) and 1.48 V (C). Experimental spectra are shown with open symbols, fitted curves with a full line. Panel (B) shows evolution of components with the electrode potential in the forward anodic (solid line) and backward cathodic (dashed line) scans. Color codes: Ir (met) (gray), Ir (III) (magenta), Ir (IV) (cyan). Panel D shows Ir4f XP spectra for the IrO_2 anode at different potentials (E-iR): 0 V (red); 0.7 V (orange); 1.3 V (yellow); 1.53 V (green); 1.56 V (cyan); 1.58 V (blue). The upper part of the panel represents the difference between the spectra obtained under different potentials and the spectrum at the open circuit conditions (0 V). Measurements were performed under 3 mbar water vapor. Kinetic energy of photoelectrons is 530 eV. Potentials are Ohmic drop corrected.

In the case of the thermal IrO_2 oxide (Figure 4D), the position, the width and the shape of the Ir4f XP spectra correspond to rutile-type IrO_2 (see Supporting Information, Figure S14) and do not change with the applied potential in the interval from 0 to 1.5 V. This is also confirmed by plotting difference spectra (upper panel of Figure 4D) obtained by subtraction of the initial

spectrum (at 0 V) from the spectra acquired at increasing anodic polarizations. The estimated atomic ratio of lattice oxygen (O1s component at 530 eV) to Ir (overall intensity of Ir4f XP spectra), equals to 2.2, which is in agreement with the IrO_2 oxide composition. Lowering the photon energy did not reveal any changes in the Ir4f spectra either (Figure S13). The XPS observation of the Ir (III) / Ir (IV) transition for electrochemical but not for IrO_2 thermal oxide may be explained by the confinement of the red-ox transition for the latter to surface defects resulting in very small sub-monolayer coverages of Ir (III), which cannot be detected by XP spectroscopy, while for electrochemical oxide it is likely to involve more than a monolayer. This conclusion is in agreement with the significantly smaller intensity of the red-ox peaks observed in the CV of thermal compared to electrochemical oxide in the potential interval from 0.2 to 1.3 V (Figures 1, S3 and S4).

In conclusion, we performed a comparative *operando* study using near-ambient pressure photoelectron spectroscopy and soft X-ray absorption spectroscopy during water electrolysis on membrane electrode assemblies containing electrochemically ($Ir@IrO_x$) and thermally synthesized (IrO_2) iridium oxides, which are widely used in PEM electrolyzers. The red-ox transition between Ir (IV) and Ir (III) is clearly observed for the electrochemical $Ir@IrO_x$ at potentials below ca. 1.3 V, while in the potential interval of the oxygen evolution Ir is present in the form of Ir (IV) in both materials. Thus, our results do not support Ir cation red-ox mechanism proposed in some previous publications. Analysis of the O K-edge spectra under the reaction conditions with the aid of DFT calculations reveals formation of an electrophilic oxygen species, O^{I-}, through an electrochemical step as an OER intermediate followed by a chemical step of molecular oxygen formation. This oxygen anion red-ox mechanism is universal occurring on two grossly different types of Ir anodes: electrochemical and thermal Ir oxide. The higher activity of

the former is likely related to its higher structural flexibility and to the greater involvement of sub-surface sites in electrocatalysis. The findings of this work may aid in the design of novel more active electrocatalytic materials for the anodes of PEM electrolyzers.

ASSOCIATED CONTENT

(Word Style "TE_Supporting_Information"). **Supporting Information**. Materials synthesis; Transmission electron microscopy images; X-ray powder diffraction patterns; electrochemical characterization in liquid electrolyte and under water vapor ambient; *in situ* spectroscopic measurement protocol, O K-edge analysis, O1s and Ir4f XP spectra analysis, DFT calculations.

AUTHOR INFORMATION

Notes

The authors declare no competing financial interests.

ACKNOWLEDGMENT

The research leading to these results has received funding from the European Union's Seventh Framework Programme (FP7/2007-2013) for Fuel Cell and Hydrogen Joint Technology Initiative under Grant No. 621237 (INSIDE). D.T. acknowledges the financial support by DFG through the priority program SPP1613. The authors thank Corinne Ulhaq-Bouillet (Strasbourg, France) for STEM measurements, Alexandr G. Oshchepkov (Novosibirsk, Russia) for his assistance during the synchrotron measurements, Helmholtz-Zentrum Berlin für Materialien und Energie for the allocation of the synchrotron radiation beamtime. T. E. J. acknowledges the Alexander-von-Humboldt Foundation for financial support. We thank Höchstleistungsrechenzentrum Stuttgart (HLRS) for access to the supercomputer HazelHen.

REFERENCES

(1) Lettenmeier, P.; Wang, R.; Abouatallah, R.; Helmly, S.; Morawietz, T.; Hiesgen, R.; Kolb, S.; Burggraf, F.; Kallo, J.; Gago, A. S.; et al. Durable Membrane Electrode Assemblies for Proton Exchange Membrane Electrolyzer Systems Operating at High Current Densities. *Electrochim. Acta* **2016**, *210*, 502–511.

(2) Lettenmeier, P.; Wang, L.; Golla-Schindler, U.; Gazdzicki, P.; Cañas, N. A.; Handl, M.; Hiesgen, R.; Hosseiny, S. S. S.; Gago, A. S.; Friedrich, A. K. Nanosized IrOx-Ir Catalyst with Relevant Activity for Anodes of PEM Electrolysis Produced by a Cost-Effective Procedure. *Angew. Chemie* **2015**, *128*, 752–756.

(3) Nong, H. N.; Oh, H.-S.; Reier, T.; Willinger, E.; M.G., W.; Petkov, V.; Teschner, D.; Strasser, P. Oxide-Supported IrNiO(x) Core-Shell Particles as Efficient, Cost-Effective, and Stable Catalysts for Electrochemical Water Splitting. *Angew. Chemie Int. Ed.* **2015**, *2* (54 (10)), 2975–2979.

(4) Abbott, D. F.; Lebedev, D.; Waltar, K.; Povia, M.; Nachtegaal, M.; Fabbri, E.; Cope, C.; Schmidt, T. J. Iridium Oxide for the Oxygen Evolution Reaction: Correlation between Particle Size, Morphology, and the Surface Hydroxo Layer from Operando XAS. *Chem. Mater.* **2016**, *28*, 6591–6604.

(5) Kötz, R.; Neff, H.; Stucki, S. Anodic Iridium Oxide Films. XPS-Studies of Oxidation State Changes and O2-Evolution. *J. Electrochem. Soc.* **1984**, *131* (1), 72–77.

(6) Kasian, O.; Grote, J. P.; Geiger, S.; Cherevko, S.; Mayrhofer, K. J. J. The Common Intermediates of Oxygen Evolution and Dissolution Reactions during Water Electrolysis on Iridium. *Angew. Chemie - Int. Ed.* **2018**, *57*, 2488–2491.

(7) Sanchez Casalongue, H. G.; Ng, M. L.; Kaya, S.; Friebel, D.; Ogasawara, H.; Nilsson, A.

In Situ Observation of Surface Species on Iridium Oxide Nanoparticles during the Oxygen Evolution Reaction. *Angew. Chemie Int. Ed.* **2014**, *53* (28), 7169–7172.

(8) Minguzzi, A.; Lugaresi, O.; Achilli, E.; Locatelli, C.; Vertova, A.; Ghigna, P.; Rondinini, S. Observing the Oxidation State Turnover in Heterogeneous Iridium-Based Water Oxidation Catalysts. *Chem. Sci.* **2014**, *5*, 3591–3597.

(9) Pfeifer, V.; Jones, T. E.; Velasco Vélez, J. J.; Arrigo, R.; Piccinin, S.; Hävecker, M.; Knop-Gericke, A.; Schlögl, R. In Situ Observation of Reactive Oxygen Species Forming on Oxygen-Evolving Iridium Surfaces. *Chem. Sci.* **2017**, *8*, 2143–2149.

(10) Mueller, D. N.; Machala, M. L.; Bluhm, H.; Chueh, W. C. Redox Activity of Surface Oxygen Anions in Oxygen-Deficient Perovskite Oxides during Electrochemical Reactions. *Nat. Commun.* **2015**, *6*, 6097–6105.

(11) Kötz, R.; Lewerenz, H. J.; Stucki, S. XPS Studies of Oxygen Evolution on Ru and RuO2 Anodes. *J. Electrochem. Soc.* **1983**, *130* (4), 825–829.

(12) Wohlfahrt-Mehrens, M.; Heitbaum, J. Oxygen Evolution on Ru and RuO2 Electrodes Studied Using Isotope Labelling and on-Line Mass Spectrometry. *J. Electroanal. Chem. Interfacial Electrochem.* **1987**, *237*, 251–260.

(13) Danilovic, N.; Subbaraman, R.; Chang, K. C.; Chang, S. H.; Kang, Y. J.; Snyder, J.; Paulikas, A. P.; Strmcnik, D.; Kim, Y. T.; Myers, D.; et al. Activity-Stability Trends for the Oxygen Evolution Reaction on Monometallic Oxides in Acidic Environments. *J. Phys. Chem. Lett.* **2014**, *5* (14), 2474–2478.

(14) Kolotyrkin, Y. M.; Losev, V. V; Chemodanov, A. N. Relationship between Corrosion Processes and Oxygen Evolution on Anodes Made from Noble Metals and Related Metal Oxide Anodes. *Mater. Chem. Phys.* **1988**, *19*, 1–95.

(15) Iwakura, C.; Hirao, K.; Tamura, H. Anodic Evolution of Oxygen on Ruthenium in Acidic Solutions. *Electrochim. Acta* **1977**, *22* (4), 329–334.

(16) Birss, V. I.; Bock, C.; Elzanowska, H. Hydrous Ir Oxide Films: The Mechanism of the Anodic Prepeak Reaction. *Canandian J Chem* **1997**, *75*, 1687–1693.

(17) Burke, L. D.; Whelan, D. P. A Voltammetric Investigation of the Charge Storage Reactions of Hydrous Iridium Oxide Layers. *J Electroanal Chem* **1984**, *162*, 121–141.

(18) Saveleva, V. A.; Wang, L.; Luo, W.; Zafeiratos, S.; Ulhaq-Bouillet, C.; Gago, A. S.; Friedrich, K. A.; Savinova, E. R. Uncovering the Stabilization Mechanism in Bimetallic Ruthenium–Iridium Anodes for Proton Exchange Membrane Electrolyzers. *J. Phys. Chem. Lett.* **2016**, *7*, 3240–3245.

(19) Law, Y. T.; Zafeiratos, S.; Neophytides, S. G.; Orfanidi, A.; Costa, D.; Dintzer, T.; Arrigo, R.; Gericke, K.; Schlögl, R.; Savinova, E. R.; et al. In Situ Investigation of Dissociation and Migration Phenomena at the Pt/electrolyte Interface of an Electrochemical Cell. *Chem. Sci.* **2015**, *6*, 5635–5642.

(20) Conway, B. E. E.; Mozota, J. Surface and Bulk Processes at Oxidized Iridium electrodes—II. Conductivity-Switched Behaviour of Thick Oxide Films. *Electrochim. Acta* **1983**, *28* (1), 9–16.

(21) Jovanovi, P.; Hodnik, N.; Ruiz-Zepeda, F.; Arcon, I.; Jozinovi, B.; Bele, M.; Šala, M.; Šelih, V. S.; Hocevar, S. B.; Gaberscek, M. Electrochemical Dissolution of Iridium and Iridium Oxide Particles in Acidic Media : Transmission Electron Microscopy , Electrochemical Flow Cell Coupled to Inductively Coupled Plasma Mass Spectrometry and X-Ray Absorption Spectroscopy Study. *J. Am. Chem. Soc.* **2017**, *139* (36), 12837–12846.

(22) Giannozzi, P.; Baroni, S.; Bonini, N.; Calandra, M.; Car, R.; Cavazzoni, C.; Ceresoli, D.; Chiarotti, G. L.; Cococcioni, M.; Dabo, I.; et al. QUANTUM ESPRESSO : A Modular and Open-Source Software Project for Quantum Simulations of Materials. *J Phys. Condens Matter* **2009**, *21*, 395502–395521.

(23) Gougoussis, C.; Calandra, M.; Seitsonen, A. P.; Mauri, F. First-Principles Calculations of X-Ray Absorption in a Scheme Based on Ultrasoft Pseudopotentials: From α-Quartz to High-Tc Compounds. *Phys. Rev. B* **2009**, *80*, 075102–075110.

(24) Taillefumier, M.; Cabaret, D.; Flank, A.; Mauri, F. X-Ray Absorption near-Edge Structure Calculations with the Pseudopotentials: Application to the K Edge in Diamond and Alpha -Quartz. *Phys. Rev. B* **2002**, *66*, 195107–195115.

(25) Trasatti, S. Electrocatalysis in the Anodic Evolution of Oxygen and Chlorine. *Electrochim. Acta* **1984**, *29* (11), 1503–1512.

(26) Pfeifer, V.; Piccinin, S.; Pfeifer, V.; Jones, T. E.; Wrabetz, S. Reactive Oxygen Species in Iridium-Based OER Catalysts. *Chem. Sci.* **2016**, *7* (August), 6791–6795.

(27) Elzanowska, H.; Birss, V. I. Reversible Ageing of Iridium Oxide Electrodes in Acidic Solutions. *J. Appl. Electrochem.* **1999**, *23* (1993), 646–654.

(28) Werner, W. S. M.; Smekal, W.; Hisch, T.; Himmelsbach, J.; Powell, C. J. Simulation of Electron Spectra for Surface Analysis (SESSA) for Quantitative Interpretation of (Hard) X-Ray Photoelectron Spectra (HAXPES). *J. Electron Spectros. Relat. Phenomena* **2013**, *190*, 137–143.

(29) Powell, C. J.; Werner, W. S. M.; Shard, A. G.; Castner, D. G. Evaluation of Two Methods for Determining Shell Thicknesses of Core−Shell Nanoparticles by X-ray Photoelectron Spectroscopy. *J. Phys. Chem. C* **2016**, *120* (39), 22730–22738.